# Precipitation, sublimation, and snow drift in the Antarctic Peninsula region from a regional atmospheric model

N. P. M. van Lipzig,[1] J. C. King, and T. A. Lachlan-Cope
British Antarctic Survey, Cambridge, UK

M. R. van den Broeke
Institute for Marine and Atmospheric Research, University of Utrecht, Utrecht, Netherlands

Received 27 February 2004; revised 23 August 2004; accepted 30 August 2004; published 23 December 2004.

[1] A regional atmospheric model, with a horizontal grid spacing ($\Delta x$) of 14 km, is used to study the surface mass balance components (precipitation, sublimation, and snow drift) in the region of the Antarctic Peninsula (AP). An integration is performed for the 7-year period 1987–1993, using a realistic forcing at the lateral model boundaries and at the sea surface. Output from this integration indicates that the precipitation reaches its maximum value on the northwestern slope of the AP, where the upward motion in the atmosphere is largest. Uplift occurs upstream of the barrier, affecting the precipitation distribution over sea. The effect of the barrier on the precipitation distribution over the Bellingshausen Sea might have important implications for the ocean circulation in this region. The mean precipitation over the grounded ice of the AP (1.20 m water eq $yr^{-1}$) is 6 times larger than the mean value over all the grounded ice of Antarctica. Our estimates for the surface sublimation and wind transport of snow over the grounding line toward the sea are 9% and 6 ± 1% of the precipitation, respectively. In situ data of the wind distribution at three coastal sites located on the northern, eastern, and western sides of the AP are used to evaluate the modeled wind field, which is important for the snow drift calculations. For two of the three sites considered, the prevailing wind direction and bimodal wind distribution are correctly represented by the model. The calculated distribution of accumulation and ablation due to snow drift shows a complex pattern. The wind removes snow from the spine of the AP, where the near-surface flow field diverges, whereas deposition occurs mainly on the eastern slopes, where the near-surface flow field converges. An intercomparison between two 7-year integrations at different horizontal resolution ($\Delta x$ = 14 km and $\Delta x$ = 55 km) shows that the precipitation on the northwestern slope is very sensitive to the model resolution: In the $\Delta x$ = 14 km integration, precipitation on the northwestern slope is higher than in $\Delta x$ = 55 km because of higher vertical velocities, resulting in a 35% increase in average precipitation over the grounded ice of the AP. *INDEX TERMS:* 3210 Mathematical Geophysics: Modeling; 3309 Meteorology and Atmospheric Dynamics: Climatology (1620); 3329 Meteorology and Atmospheric Dynamics: Mesoscale meteorology; 3349 Meteorology and Atmospheric Dynamics: Polar meteorology; 3354 Meteorology and Atmospheric Dynamics: Precipitation (1854); *KEYWORDS:* precipitation, Antarctic Peninsula, regional atmospheric model

**Citation:** van Lipzig, N. P. M., J. C. King, T. A. Lachlan-Cope, and M. R. van den Broeke (2004), Precipitation, sublimation, and snow drift in the Antarctic Peninsula region from a regional atmospheric model, *J. Geophys. Res.*, *109*, D24106, doi:10.1029/2004JD004701.

## 1. Introduction

[2] Information on the spatial and temporal variability of the surface mass balance ($B$) in the Antarctic Peninsula region is required for several purposes. First, interpretation of ice and firn cores can be improved by detailed knowledge of temporal variations in $B$, defined as the sum of precipitation, evaporation, sublimation, snow drift and runoff [e.g., *Werner et al.*, 2000, *van Lipzig et al.*, 2002a]. Since the Antarctic Peninsula (AP) is a region with a high density of ice and firn cores, which contain fundamental information on past changes in meteorological variables, it is important to improve our understanding of processes that affect $B$ in this region. Second, the AP is a relatively important con-

[1]Now at Meteorological Institute, University of Munich, Munich, Germany.


0148-0227/04/2004JD004701$09.00

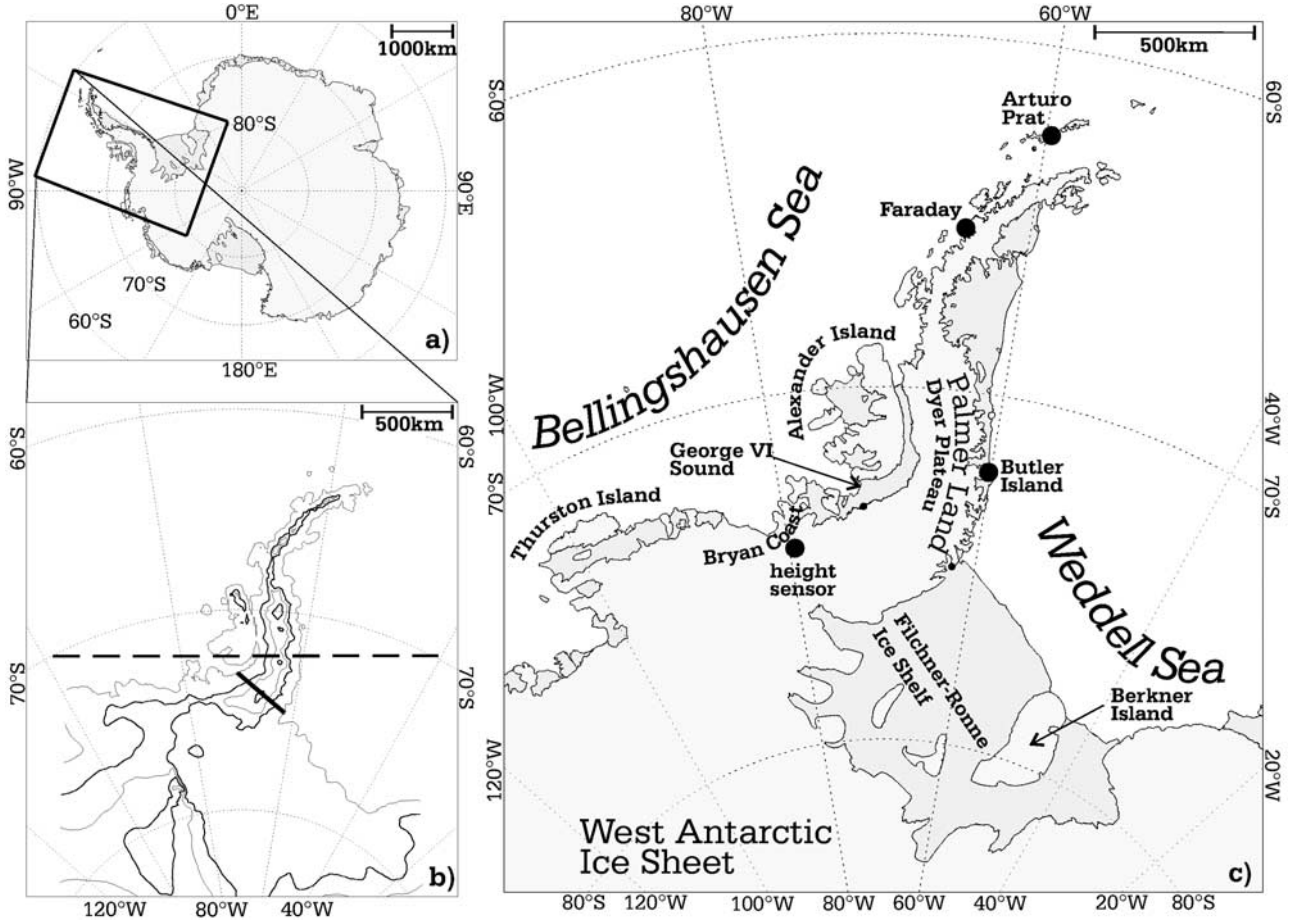


**Figure 1.** (a) Domain covered by the regional model. (b) Model surface elevation of the Antarctic Peninsula. Contours are plotted at surface elevations of 50 m and 1.5 km (thin lines) and 1 and 2 km (thick lines). The thick solid line joining Cape Adams and a point (73°24′S, 72°00′W) on the English coast defines the Antarctic Peninsula [*Aagaard*, 1930]. The thick dashed line indicates the location of a vertical cross section shown in Figure 2. (c) Map with places referred to in the text. The land ice is identified with the light gray shading, and the ice shelves are identified with the dark gray shading.

tributor to the present-day $B$ of the entire Antarctic ice sheet. Our current estimate of annual mass input on the AP is 13% of the total mass input on the Antarctic ice sheet, whereas the area of the AP is only 3% of the total area (estimate derived from *van Lipzig et al.* [2002b]).

[3] The climate of the AP has been changing over the last 50 years. The surface mass balance has increased at isolated ice core sites [*Peel*, 1992], the number of winter precipitation ($P$) events at the station Rothera has increased by 50% [*Turner et al.*, 1997], and a number of floating ice shelves have retreated and disintegrated [*Vaughan and Doake*, 1996; *Skvarca et al.*, 1999]. These changes have occurred along with an increase in surface temperature. One of the largest temperature trends on earth over the last 50 years has been measured at the station Faraday (Figure 1c), where the annual mean temperature has increased by 2.5°C over this period [*King*, 1994]. Several factors contributing to the anomalous warming in the AP and Weddell Sea region have been proposed [*Orr et al.*, 2004; *Marshall et al.*, 2002; *van den Broeke and van Lipzig*, 2003], some of them related to the increase in westerlies, observed over the last 30 years [*Marshall*, 2002].

[4] The AP consists of a 1500 km long and about 2 km high mountain range. The orographic barrier has an important effect on the $P$ and temperature ($T$) distribution. Different $P$ and $T$ regimes are found on either side of the AP [*Turner et al.*, 2002; *King and Comiso*, 2003].

[5] It is difficult to perform accurate and spatially representative measurements of $P$ in mountainous regions. In Antarctica, where $P$ falls in solid form under high wind speed conditions, conventional rain gauges are unsuitable. Therefore net accumulation is measured instead of $P$, using stakes, ice or firn cores. The major problem is that these measurements are affected by transport of snow by the wind, which is highly variable on a small scale. Another problem is that melt can play a significant role at lower elevation.

[6] The first detailed map of $B$ in the AP region has recently been derived by *Turner et al.* [2002] using about 200 stake, ice core and firn core measurements. Uncertainties in this map are large because the measurement sites are irregularly distributed. $B$/height relationships for different sections of the AP were used to control the interpolation of the measurements. To obtain a more

physically based knowledge of $B$ in this mountainous terrain an alternative method is required.

[7] In the past, the European Centre for Medium-Range Weather Forecasts Re-Analyses (ERA15) have been used to derive the spatial distribution of $P$ in the AP region [*Turner et al.*, 1999, 2002] and the temporal variability at specific sites [*Marshall*, 2000]. While the resolution of ERA15 (T106) and ERA40 (T159) is impressive on the global scale, it is not high enough to represent the AP accurately. For example, the height of the northern spine is underestimated by about 70% and the height of the Dyer Plateau by 30% [*Turner et al.*, 2002]. As a result, too many depressions cross the AP in ERA15, rather than being blocked on the western side. The coarse resolution and smoothing of the orography result in elevations larger than zero over sea. Therefore an unrealistic westward displacement of $P$ is found and the accumulation gradient is weaker than the measurements indicate. In addition, the model fields are found to have peak values of precipitation minus sublimation minus evaporation ($P - E$) of only half the measured values. Note that sublimation on the AP is much larger than evaporation. We will refer to the net surface water vapor flux (sum of evaporation and sublimation) as $E$.

[8] To obtain more accurate information on the distribution of $B$ over the AP, model integrations at a high horizontal resolution are necessary. The goal of this paper is to study the spatial and temporal variability of the separate components of the $B$ namely $P$, $E$ and snow drift ($SN$) and to derive an area average estimate for the grounded ice of the AP. As a tool, we use a regional atmospheric model at 14 km resolution, realistically driven from the lateral boundaries. In this paper, we do not consider melt and sublimation of blowing snow. Melt is important locally in coastal regions. The parameterization of sublimation of blowing snow [e.g., *Bintanja and Reijmer*, 2001] has not yet been implemented in our code. *Déry and Yau* [2002] estimated sublimation of blowing snow to be about equal to $E$. On the other hand, *King et al.* [1996] and *Mann et al.* [2000] showed that during the sublimation of blowing snow a layer of near-saturated air forms, resulting in a negative feedback, which limits the blowing snow sublimation.

[9] Over the last decade, high-resolution regional models have been used successfully to study precipitation processes in different mountainous regions of the world, for example the South Island of New Zealand [*Katzfey*, 1995], the Olympic mountains, USA [*Colle and Mass*, 1996], the European Alps [*Frei et al.*, 2003] and Greenland [e.g., *Kiilsholm et al.*, 2003; *Box and Rinke*, 2003]. These studies indicate $P$ formation in the lower troposphere through forced ascent, resulting in a maximum value of $P$ over the upwind slopes and a leeward rain shadow. Studies on the sensitivity of $P$ to model resolution show clear benefits in increasing the resolution in regions where circulation is forced by the orography [*Mass et al.*, 2002].

[10] Case studies of the atmospheric flow in the AP region with a high-resolution 'state of the art' model have been performed previously [*Pascoe*, 2002; *Orr et al.*, 2004]. However, our study is the first study where an integration of several years has been performed to obtain climatological information for this region at a horizontal resolution of 14 km.

## 2. Description of the Model

[11] We have used a regional atmospheric model (RACMO14), with a horizontal grid spacing ($\Delta x$) of 14 km and 20 levels in the vertical, to simulate the climate of the AP for the 7-year period 1987–1993. The model is driven from the lateral boundaries by output from an integration with essentially the same model at coarser resolution (RACMO55; $\Delta x = 55$ km). At the lateral boundaries, the relaxation method of *Davies* [1976] is used. The RACMO55 integration, which is driven from the lateral boundaries by ERA15, is described in detail by *van Lipzig et al.* [2002b]. Sea surface temperature and sea-ice extent in both RACMO14 and RACMO55 are prescribed from observations.

[12] The RACMO model uses the dynamical part of the HIgh-Resolution Limited Area Model (HIRLAM) and the physical parameterizations of the ECHAM-4 model [*Roeckner et al.*, 1996]. A detailed description of the model is given by *Christensen et al.* [1996] and *Christensen and Van Meijgaard* [1992]. Several adjustments have been made to improve the model for Antarctic conditions [*van Lipzig et al.*, 1999, 2002b]. Apart from these changes, which have been implemented both in RACMO14 and in RACMO55, additional changes have been made to the RACMO14 code, namely a modification of i) the orography in the relaxation zone, ii), the formulation of cloud cover and iii), the roughness length for momentum and heat. These modifications are described below.

[13] The RACMO14 domain covers the AP, the Filchner-Ronne Ice Shelf, parts of the Weddell Sea, Bellingshausen Sea and the West Antarctic Ice Sheet (Figure 1a). Part of the lateral boundary zone, is located over the complex orography of the West Antarctic Ice Sheet. The small-scale orography is better resolved for $\Delta x = 14$ km than for $\Delta x = 55$ km. For example, the mountain range of Thurston Island, located in the lateral boundary zone, is resolved by the high- but not by the low-resolution grid. This difference in orography between the models, resulted in unrealistic RACMO14 output. The RACMO55 fields, that were used to force the RACMO14 integration from the lateral boundaries, were inconsistent with the RACMO14 orography. To solve this problem, the RACMO55 orography was interpolated to the RACMO14 grid. In the lateral boundary zone of RACMO14, the interpolated RACMO55 orography was used. For the ten adjacent points, a weighted mean of the interpolated RACMO55 and RACMO14 orography was used to create a smooth transition between coarse and high-resolution orography. This adjustment clearly improved the RACMO14 output.

[14] The ECHAM4 parameterization of subgrid-scale cloud formation [*Roeckner et al.*, 1996] is an adjusted version of the scheme developed by *Sundqvist* [1978]. The evolution of temperature, specific humidity ($q_v$) and cloud water/ice ($q_w$) is calculated in the cloudy and in the cloud free part of a grid box. Cloud cover ($b$) is diagnosed from grid box average values. Condensation of $q_v$ and evaporation of $q_w$ occurs in the cloudy part of the grid box. In the cloud free part evaporation occurs; $q_w$ transported into this part of the grid box is evaporated instantaneously and precipitation

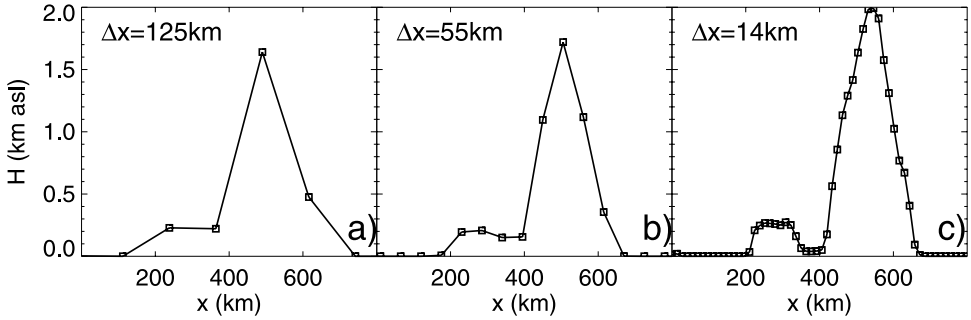


**Figure 2.** Vertical cross section (along the dashed line indicated in Figure 1b) of the model elevation at different grid spacing, namely, (a) $\Delta x$ = 125 km, (b) $\Delta x$ = 55 km, and (c) $\Delta x$ = 14 km. Every point refers to a model grid point.

falling into this part of the grid box is evaporated as a function of the saturation deficit. The variable $q_w$ is prognostic, but the phase of $q_w$ is diagnosed as a function of temperature. The autoconversion of cloud droplets to precipitating raindrops is parameterized as a function of in-cloud water content taking into account the collision of cloud droplets with larger raindrops. The terminal velocity of ice crystals is parameterized in terms of in-cloud ice water content, with the loss of ice crystals due to sedimentation given by the divergence of the ice water flux density.

[15] In the original scheme, $b$ is parameterized as a function of grid box mean relative humidity, with a condensation threshold depending on the height above the surface. When testing the model at $\Delta x$ = 14 km, it appeared that during some cases when the relative humidity is close to the threshold value, oscillations occurred in $b$, $q_v$ and $q_w$. We replaced the original ECHAM4 formulation by a new formulation in which $b$ was parameterized as a function of total water ($q_w + q_v$) as described by *Lenderink and Van Meijgaard* [2001]. They showed that the combination of a moist turbulence scheme and a cloud fraction formulation based on relative humidity gives rise to unrealistic feedbacks. Moreover, a recent model intercomparison study of boundary layer clouds showed that the intermittency of $b$ and $q_w + q_v$ is a general feature in many models, with the feedback between turbulence and clouds being a key factor [*Lenderink et al.*, 2004]. In our model integrations, problems related to spurious oscillations in $b$, $q_v$ and $q_w$ were solved by implementing the formulation of *Lenderink and Van Meijgaard* [2001].

[16] *Van Lipzig et al.* [2002b] and *Reijmer et al.* [2004] showed that $E$ was overestimated in RACMO55 in mountainous regions because of an overestimation of the surface roughness length for heat and moisture ($z_{0h}$). The drag exerted on the mean flow by the orography on scales smaller than the size of a grid box is parameterized by increasing the roughness length for momentum exchange ($z_{0m}$) as a function of the subgrid-scale orography. Since in our RACMO version $z_{0h}$ is identical to $z_{0m}$, this formulation enhances sensible and latent heat exchange in the mountainous regions. *Reijmer et al.* [2004] showed that the agreement between modeled and measured surface heat fluxes in RACMO can be improved by reducing $z_{0h}$. Therefore we used a value of 1 mm for $z_{0h}$ and $z_{0m}$ in RACMO14 independent of the subgrid-scale orography.

[17] An improvement in model resolution affects the detail in which the orography of the AP is resolved, as can be seen in Figure 2, where a cross section of the surface elevation of Alexander Island and the Dyer Plateau is shown for three different model resolutions. A grid spacing of 125 km is a value typically used in high-resolution global models (e.g., ERA40). In this case, the width of the AP at about 72°S, is resolved by only four points. Only one point is present on the eastern slope and the maximum elevation is underestimated by about 20%. When $\Delta x$ = 55 km, a typical value used in regional atmospheric models (e.g., RACMO55), the width of the AP at about 72°S, is resolved by 8 points and the maximum elevation is still underestimated. A dip in elevation is present at the location of George VI Sound, but the elevation of this ice shelf is overestimated. Using $\Delta x$ = 14 km (this study), the width of the AP at about 72°S, is resolved by 35 points, the steep slopes are resolved by 8 points and George VI Sound is at zero elevation. It is clear that a resolution of 14 km is sufficient to resolve the steep slopes and the height of the barrier. This means that the uplift induced by the steep orographic barrier is taken into account, which is very important for modeling $P$.

## 3. Results

### 3.1. Precipitation Minus Sublimation

[18] Our current knowledge of the spatial distribution of $B$ in the AP region is based on 200 stake, ice core and firn core measurements. *Turner et al.* [2002] have used these measurements to derive an accumulation map for the AP (Figure 3a). Together with the in situ measurements, they have used $B$/height relationships for different regions of the AP. High values, larger than 2 m water eq (w.e.) yr$^{-1}$, are found on the northern spine and on top of the mountains on Alexander Island. The dyer plateau and the southeastern part of the AP are relatively dry.

[19] The large-scale distribution of $B$, is mainly determined by $P - E$. We therefore focus on these two components of $B$ in this subsection. Transport of snow by the wind will be discussed in Section 3.3. Figure 3b shows the 7-year mean climatological RACMO14 $P - E$ for the period 1987–1993. The distribution is similar to Turner's map with high values, larger than 2 m w.e. yr$^{-1}$, in the northwest and lower values in the southeast of the AP. There

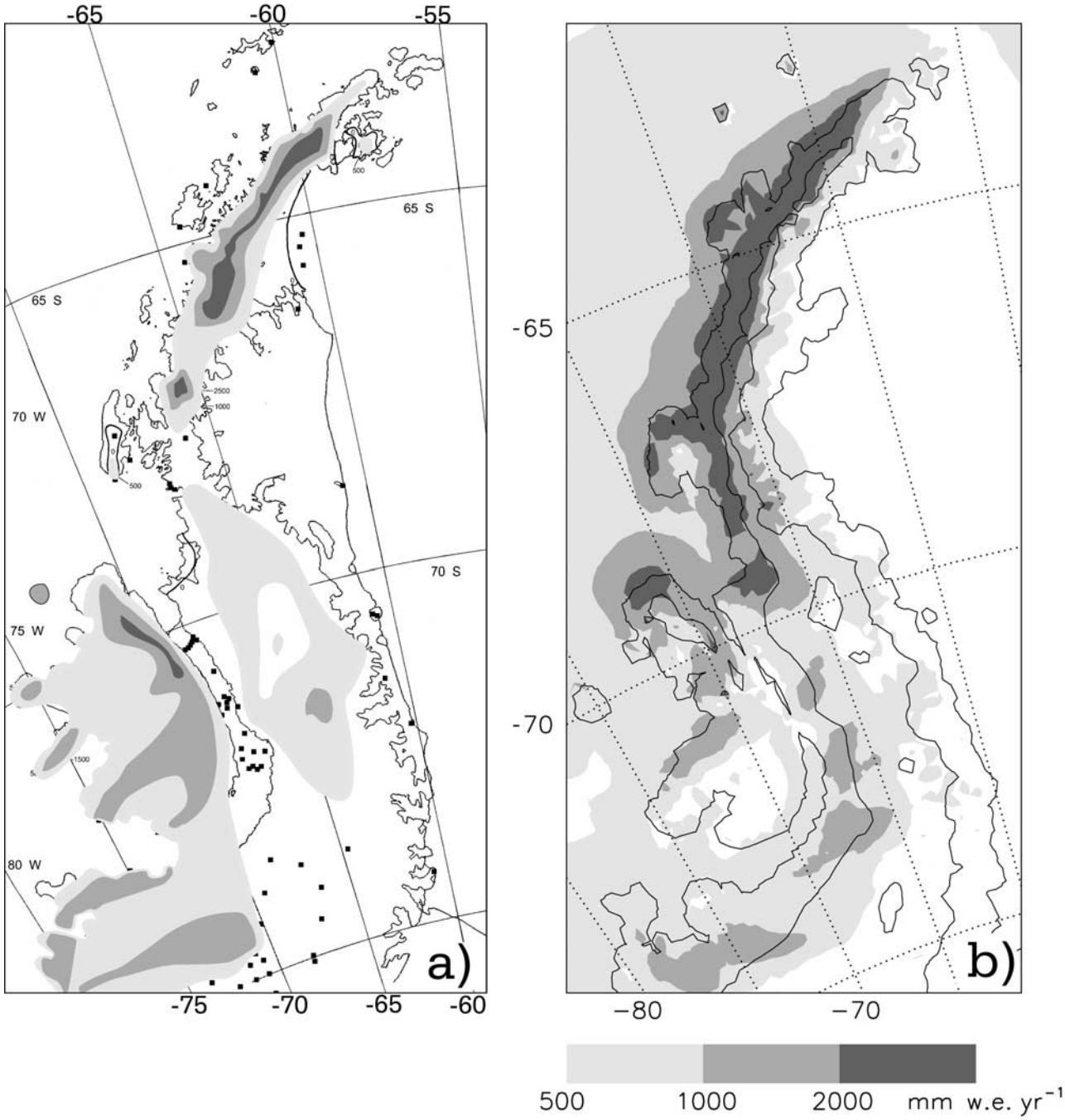


**Figure 3.** Climatological surface mass balance. (a) Compilation derived from about 200 stake, ice core, and firn core measurements [*Turner et al.*, 2002]. Black contour lines indicate the edge of the ice shelf and the grounding line. (b) RACMO14 precipitation minus sublimation ($P - E$) for the period 1987–1993. Contour lines are plotted at model surface elevations of 50 m, 1 km, and 2 km.

are, however, also remarkable differences between the maps. In the model, the maximum value for $P$ is found on the northwestern slope of the AP, whereas Turner's map shows the highest values on the northern spine. It cannot be determined whether the location of the maximum in $P$ on the northwestern slopes is correctly represented by the model, since there are no measurements to evaluate the model in this region, and Turner's map relies heavily on the empirical $B$/height relationship. Model output shows larger differences between the east and the west side of the AP (and the north and south of Alexander Island) than the measurements indicate.

[20] Data are sparse in the AP, especially in northern regions. Apart from the sites near the coast, there is only one measuring site north of 60°N. Interpolation of the sparse measurements is uncertain. To exclude the effect of the interpolation, we compare model output directly with the in situ measurements. The relative RACMO14 deviation from the observed value for $B$ ($B_{obs}$) is plotted in Figure 4. The bias at a site ($\Delta B$) is defined as the modeled value for $B$

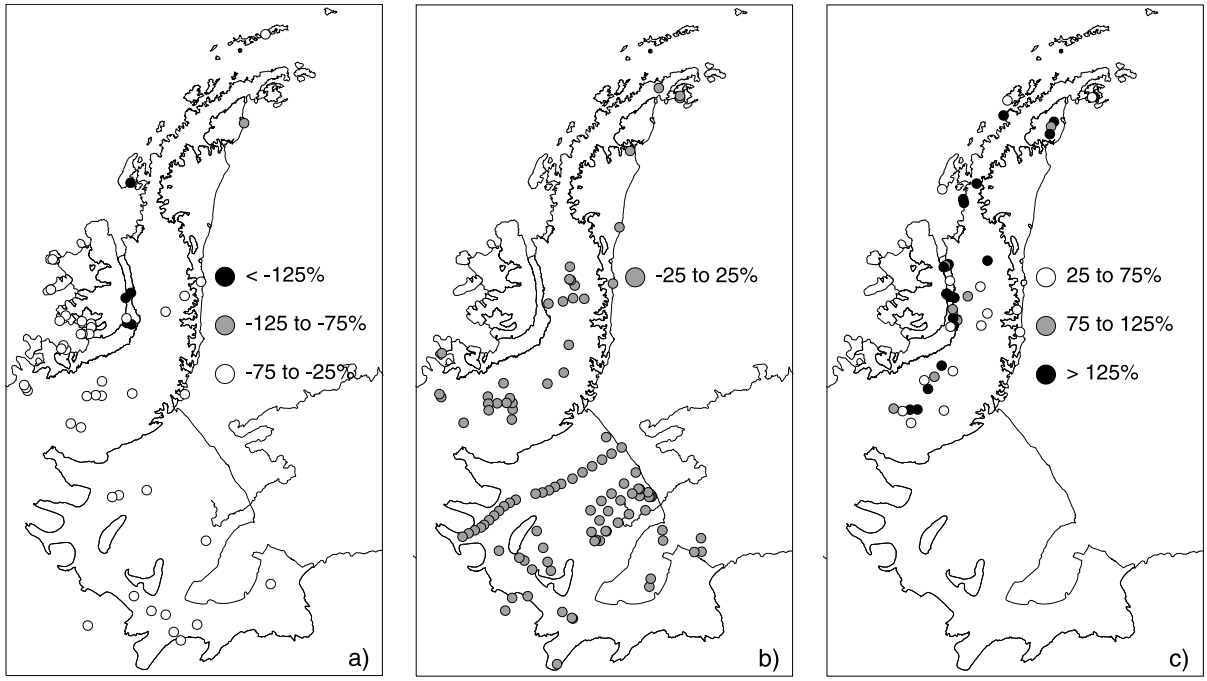


**Figure 4.** Difference ($\Delta B$) in percentage terms between the measured surface mass balance ($B_{obs}$) and the modeled surface mass balance ($B_{mod}$), here defined as $P - E$: (a) $\Delta B/B_{obs} < -25\%$, (b) $-25\% \leq \Delta B/B_{obs} \leq 25\%$, and (c) $25\% < \Delta B/B_{obs}$.

($B_{mod}$) minus $B_{obs}$. The mean bias over all in situ measurements available is given by;

$$\langle \Delta B \rangle = \frac{1}{N} \sum_{i=1,N} (B_{mod} - B_{obs}), \quad (1)$$

where $N$ is the number of in situ measurements. For the 200 measurements available, $\langle \Delta B \rangle$ is $-9$ mm w.e. yr$^{-1}$, which is only 2% of $\langle B_{obs} \rangle$. This value is smaller that the uncertainty in the measurements.

[21] The mean absolute bias, which is defined as;

$$\langle |\Delta B| \rangle = \frac{1}{N} \sum_{i=1,N} |(B_{mod} - B_{obs})|, \quad (2)$$

is 220 mm w.e. yr$^{-1}$. Part of this bias is related to snow drift on a scale smaller than the size of a grid box. Sites, which are separated by only a few km, often show large differences in accumulation. A threefold increase in $B$ can be observed over a distance of only 10km [*Turner et al.*, 2002]. Especially in Palmer Land, the spatial variability in $\Delta B$ is large, indicating the importance of the effect of snow drift on a small scale.

[22] At 51 of the sites considered, $B_{mod}$ is underestimated by more than 25%. In the southwest of Alexander Island, the model systematically deviates from the measurements. $B_{mod}$ is clearly underestimated in this region, indicating that the leeward precipitation shadow of the mountains of Alexander Island is overestimated in the model. This might be related to the fact that $P$ is a diagnostic model variable and that advection of $P$ is not taken into account, resulting in an underestimation of spillover of $P$ on the lee side of the barrier.

[23] At 48 of the sites, $B_{mod}$ is overestimated by more than 25%. This can partly be explained by summer melt on the north western coast and on the George VI ice shelf. Melt is not taken into account in the model. At some coastal stations the entire winter snowfall melts during summer and $B$ is negative, in spite of $P$ in excess of 1 m w.e. yr$^{-1}$ [*Turner et al.*, 2002].

[24] No measurements are present on the northwestern slope. For this reason, it cannot be objectively decided whether the location of the modeled maximum in $P$ on the northwestern slope of the barrier is correctly represented. At the only site on top of the northern spine, $B$ is correctly represented by the model.

[25] At 101 of the 200 sites considered, $\Delta B$ is within the range of uncertainty of the measurements ($|\Delta B| \leq 0.25 \cdot B_{obs}$). Especially in the region of the Filchner-Ronne Ice Shelf and Berkner Island, which is more homogeneous that the AP, accumulation is very well represented by the model.

[26] To study the effect of a change in resolution on the model output, we have plotted the spatial distribution of $P - E$ in RACMO14 and in RACMO55 (Figure 5). The difference in 7-year mean $P - E$ between these two integrations is shown in Figure 6. Broad-scale features are similar in both integrations. However, over the north western slopes, $P - E$ increases with decreasing grid spacing, a result consistent with previous studies on the sensitivity of $P$ to $\Delta x$ [e.g., *Katzfey*, 1995]. Over the eastern slopes, the model output is less dependent on the model resolution than over the western slopes. In the RACMO55 integration, there is a maximum in $P - E$ over sea on the western side of the AP, followed by a local minimum and a secondary maximum higher upslope; the $P - E$ pattern on the western side of the AP is patchy. In RACMO14, the spatial distribution of $P -$

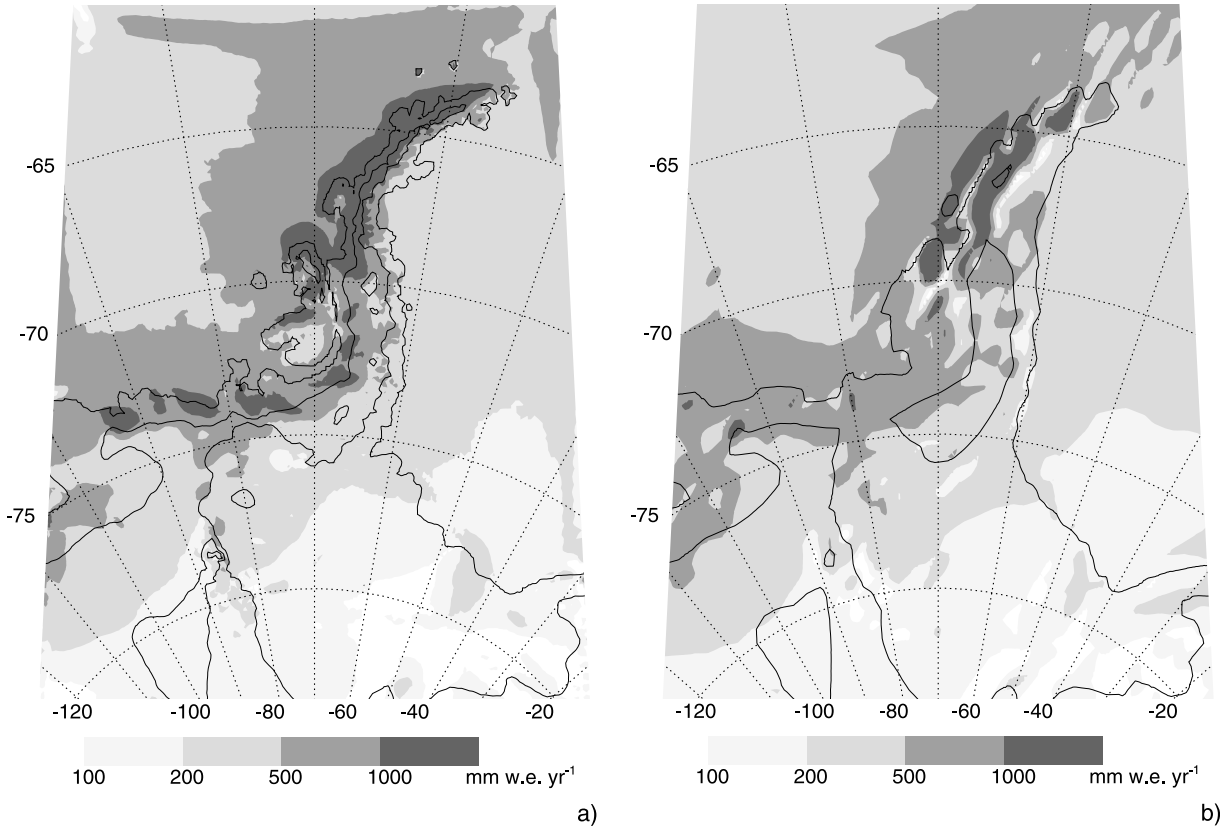


**Figure 5.** Seven-year mean (1987–1993) precipitation minus sublimation for (a) RACMO14 and (b) RACMO55.

$E$ is smoother than in RACMO55 and the local minimum is not present. The mean negative bias is larger for RACMO55 ($\langle \Delta B \rangle$ is $-65$ mm w.e. yr$^{-1}$) than for RACMO14 ($\langle \Delta B \rangle$ is $-9$ mm w.e. yr$^{-1}$) and $\langle |\Delta B| \rangle$ is smaller for RACMO55 than for RACMO14 (170 mm w.e. yr$^{-1}$ versus 220 mm w.e. yr$^{-1}$).

[27] Previous studies have indicated that, in mountainous regions, the modeled vertical velocities and consequently $P$ increase with decreasing $\Delta x$ [e.g., *Wu et al.*, 2002]. The vertical cross section of modeled vertical velocities on the northern spine is shown in Figure 7. In RACMO55 upward motion occurs at the western grounding line and downward motion at the lee side of the barrier. In RACMO14, the orography is resolved in better detail and vertical velocities are much larger than in RACMO55. A mountain wave is present, with upward motion on the windward side, downward motion on the crest and leeward side, followed by upward motion east of the barrier. This pattern of vertical velocities is tilted westward with altitude. These results are in correspondence with *Colle* [2004], who showed that mountain gravity waves can enhance upstream motion on the lower windward side of a mountain. The maximum RACMO14 value for $P$ is 3 times as large as the maximum RACMO55 value, but in both integrations, the maximum is found on the windward slope of the barrier.

[28] Vertical velocity in the atmosphere and consequently $P$ is related to the blocking of the flow by the barrier. The Froude number, which indicates whether the flow has enough kinetic energy to rise over the barrier, is defined as $Fr = U/(N_{moist}H_{barrier})$, where $U$ is the mean upstream wind speed, $H_{barrier}$ is the height of the mountain barrier, and $N_{moist}$ is the moist Brunt-Väisälä frequency as derived by *Durran and Klemp* [1982]. When $0 < Fr < 1$, the flow is blocked by the barrier and when $Fr > 1$, unblocked flow conditions prevail. To study the effect of flow blocking on the distribution of $P$, we have performed a case study for the year 1993. $Fr$ is calculated for the layer between 925 hPa and 700 hPa at a point 500 km upstream of the coast (67.1°W, 63°S). Six hourly model output for 1993 has been subdivided into two categories; i) $Fr \geq 1$, and ii) $0 < Fr < 1$. Prevailing meteorological conditions during these two types of flow conditions are shown in Figure 8. During blocked flow conditions, southerly winds prevail along the barrier and uplift and $P$ are very small. It can be concluded that the maximum in $P$ west of the spine is the result of uplift in cases of unblocked flow.

[29] The near-surface wind speed at the lowest model level (7 m) is very small near the west coast of the AP during blocked flow conditions (not shown). When the flow is unblocked for the layer between 925 hPa and 700 hPa, the near surface winds show a clear barrier wind signature [*Parish*, 1982]; the incident near-surface flow is blocked and cold air piles up against the barrier, establishing a pressure gradient with the highest pressure at the base. The associated pressure gradient force and the Coriolis force cause northerly flow parallel to the barrier at the west

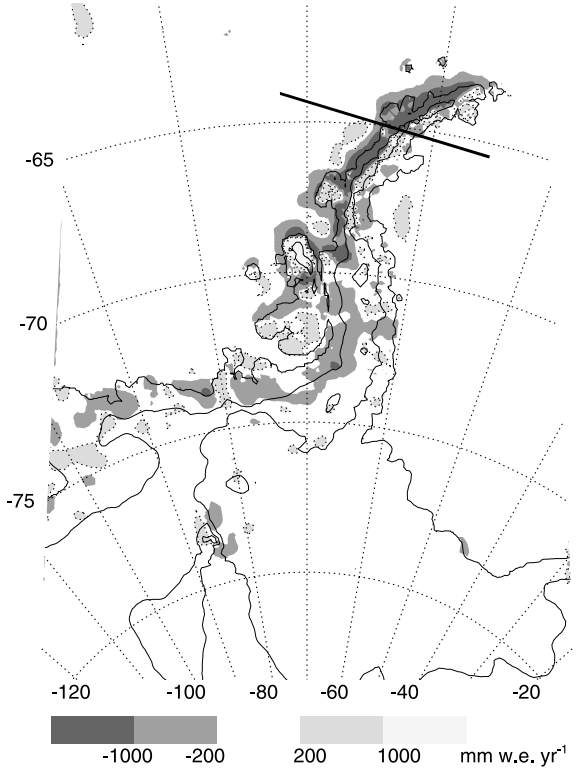


**Figure 6.** Difference between RACMO55 and RACMO14 7-year mean (1987–1993) precipitation minus sublimation ($P - E$). Dotted contours indicate positive values, where RACMO55 output is larger than RACMO14 output. The solid line indicates the location of a vertical cross section presented in Figure 7.

coast of the AP except for the northern tip of the AP, where the flow is from the south, a result also found by *Orr et al.* [2004]. This means that when $Fr > 1$ in the layer between 925 hPa and 700 hPa at a point 500 km upstream of the barrier, the flow climbs over the barrier at higher atmospheric levels, but the flow is deviated along the steep coastal mountains at lower atmospheric levels.

[30] The AP is defined as the region north of a line joining Cape Adams and a point (73°24′S, 72°00′W) on the English coast [*Aagaard*, 1930] (see Figure 1b). The surface mass balance components, averaged over this region, differ greatly between the integration at $\Delta x$ = 14 km (RACMO14) and the integration at $\Delta x$ = 55 km (RACMO55). Taking the RACMO55 integration as the reference, $P$ increases by 35% in RACMO14, due to an increase in the vertical velocity, and $E$ decreases by 25% in RACMO14, due to a decrease in $z_{0h}$. In addition, the total area of the AP decreases by 19% in RACMO14 due to a better representation of the land sea mask in the high-resolution model. In addition, $SN$ is calculated in the RACMO14 integration, and 6 ± 1% of the total precipitation is found to be transported from the land ice into sea (see section 3.3). In summary, the average value for $B_{mod}$ over the AP is 12% larger in the RACMO14 than in the RACMO55 integration.

### 3.2. Wind

[31] In the previous section, we have focused on $P$ and $E$, which are the most important components for the large-scale distribution of $B$. However, $SN$ might play a role on a smaller scale. For a good estimate of $SN$, it is necessary that the near-surface winds are correctly represented in the model. For this reason, the model wind field is compared with in situ data, obtained as part of the Scientific Committee on Antarctic Research READER (REference Antarctic Data for Environmental Research) project [*Turner et al.*, 2004]. To study whether decreasing $\Delta x$ improves the modeled wind field by a

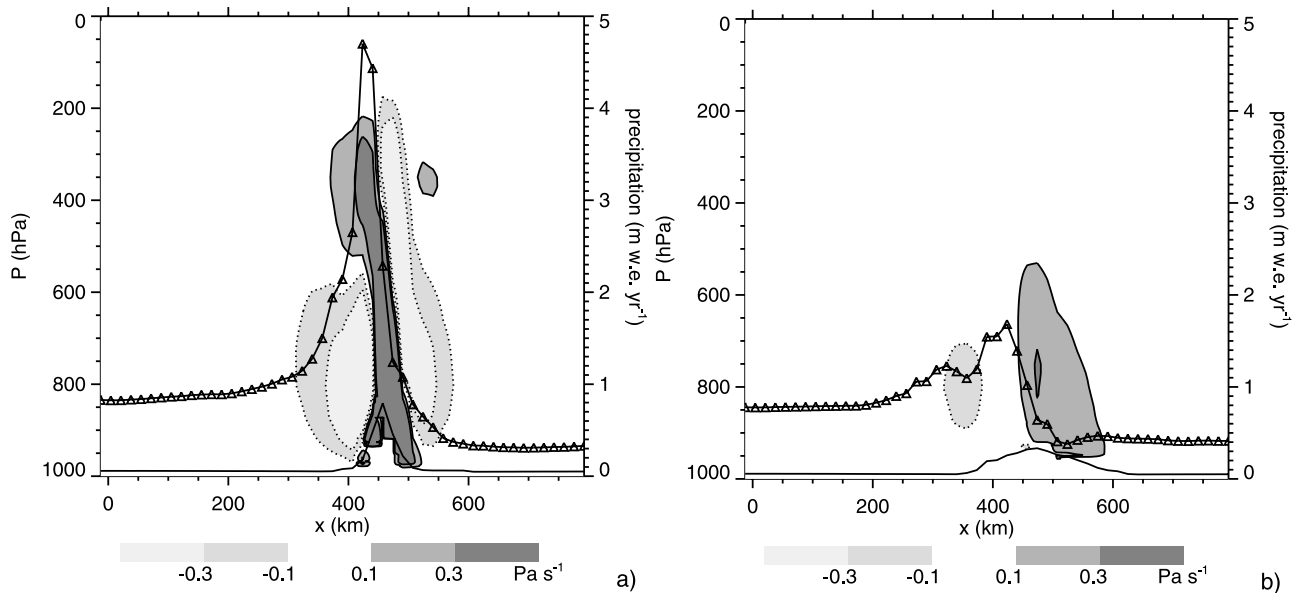


**Figure 7.** Vertical cross section of vertical velocity (shaded) and precipitation (solid line with triangles) in (a) RACMO14 and (b) RACMO55 along the line indicated in Figure 6. The solid line indicates the surface pressure.

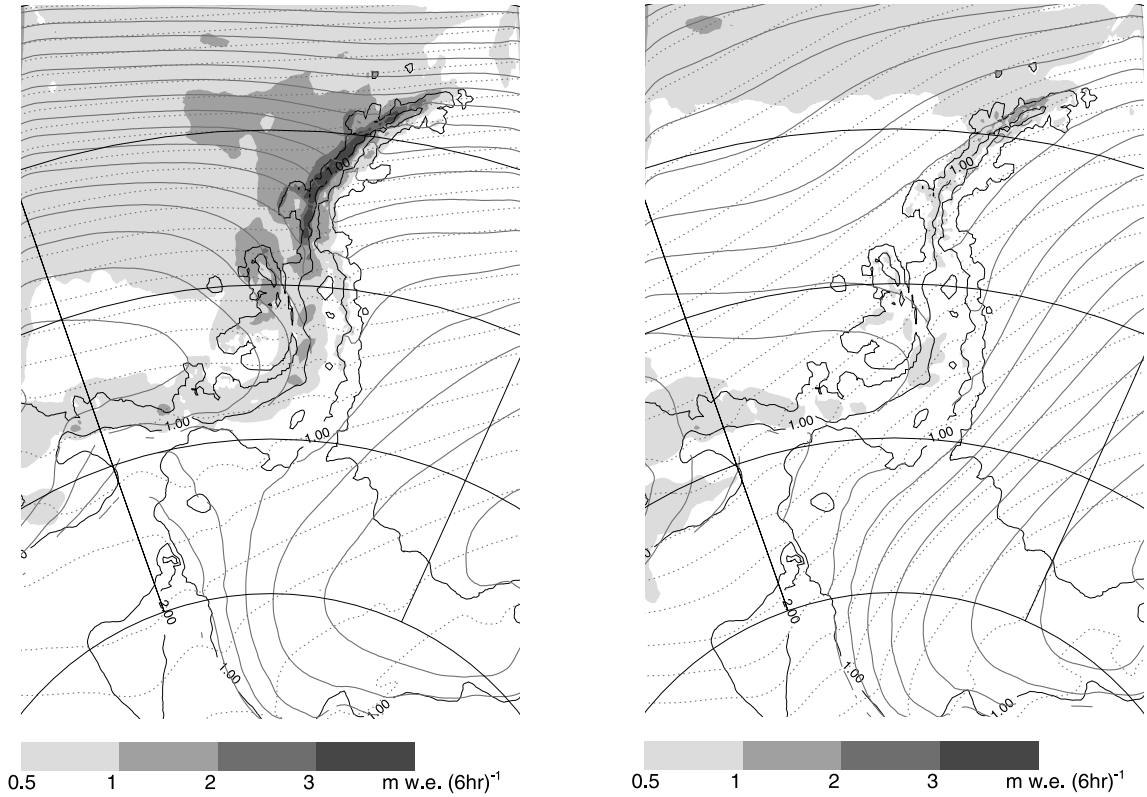


**Figure 8.** Precipitation (shaded), geopotential at 500 hPa (dashed gray lines), geopotential at 850 hPa (solid gray lines), and surface elevation (solid lines) for (a) cases in 1993 where $Fr \geq 1$ and (b) cases in 1993 where $0 < Fr < 1$. Note that the geopotential at 850 hPa is only plotted when the surface pressure is larger than 850 hPa.

better representation of the local orography, we include RACMO55 output in the evaluation.

[32] Figure 9 shows the frequency of occurrence of winds in each of 12 direction sectors during the time period 1987–1993. Both observations and model output from RACMO14 and RACMO55 are shown for three stations representing different climatic regimes. Arturo Prat is located on an island north of the AP, Faraday in complex terrain on the western side and Butler Island on the eastern side of the AP. At Arturo Prat, the bimodal wind distribution with prevailing winds from east and from west-southwest, is represented by RACMO14 but not by RACMO55. Also at the surrounding grid boxes in RACMO55 (not shown) prevailing winds are from the west, with the south-southeasterlies stronger and the easterlies weaker than the measurements indicate. North-northwesterly winds are overestimated in both RACMO14 and RACMO55, but the observed absence of southeasterly winds is better represented by RACMO14 than by RACMO55. The modeled wind speed at Arturo Prat (8.4 m $s^{-1}$) is 50% larger than the measured wind speed (5.6 m $s^{-1}$). This might be partly related to local effects. The measured wind speed at the station King Sejong (7.8 m $s^{-1}$) (located 60 km from Arturo Prat) is much higher and therefore closer to the modeled wind speed at the grid point corresponding to this station (8.9 m $s^{-1}$). Generally measurements of the wind speed are made in sheltered regions and therefore the site might experience lower wind speeds than the large-scale mean value.

[33] At Faraday, both RACMO14 and RACMO55 fail to represent the observed bimodal distribution. Also the wind speed is too high in the RACMO14 (6.5 m $s^{-1}$ instead of 4.2 m $s^{-1}$). Clearly, even a resolution of 14 km is too coarse to represent the complexity of the terrain in this region.

[34] At Butler Island, the bimodal distribution with winds from both the north and from the south (barrier effect) are represented in RACMO14. The difference between measured and modeled wind speed at this station is only 0.04 m $s^{-1}$. The bimodal distribution is not present at the RACMO55 grid point located nearest to Butler Island, but is present at a sea grid point located east of Butler Island. However, at this grid point the northerlies are underestimated. It is clear that RACMO14 is superior in representing the observed winds at the stations compared with RACMO55 and is therefore better suitable to study *SN* in the AP.

### 3.3. Snow Drift

[35] The transport of snow by the wind ($Q$) is related to the near-surface wind speed or the friction velocity ($u_*$), defined as the square root of the kinematic surface stress. Empirical relations between $Q$ and the near-surface wind speed or $u_*$ have been used previously to estimate *SN* from modeled near surface wind fields on different spatial scales [*van den Broeke and Bintanja*, 1995; *Déry and Yau*, 2002]. We use a parameterization [*Mann et al.*, 2000] based on

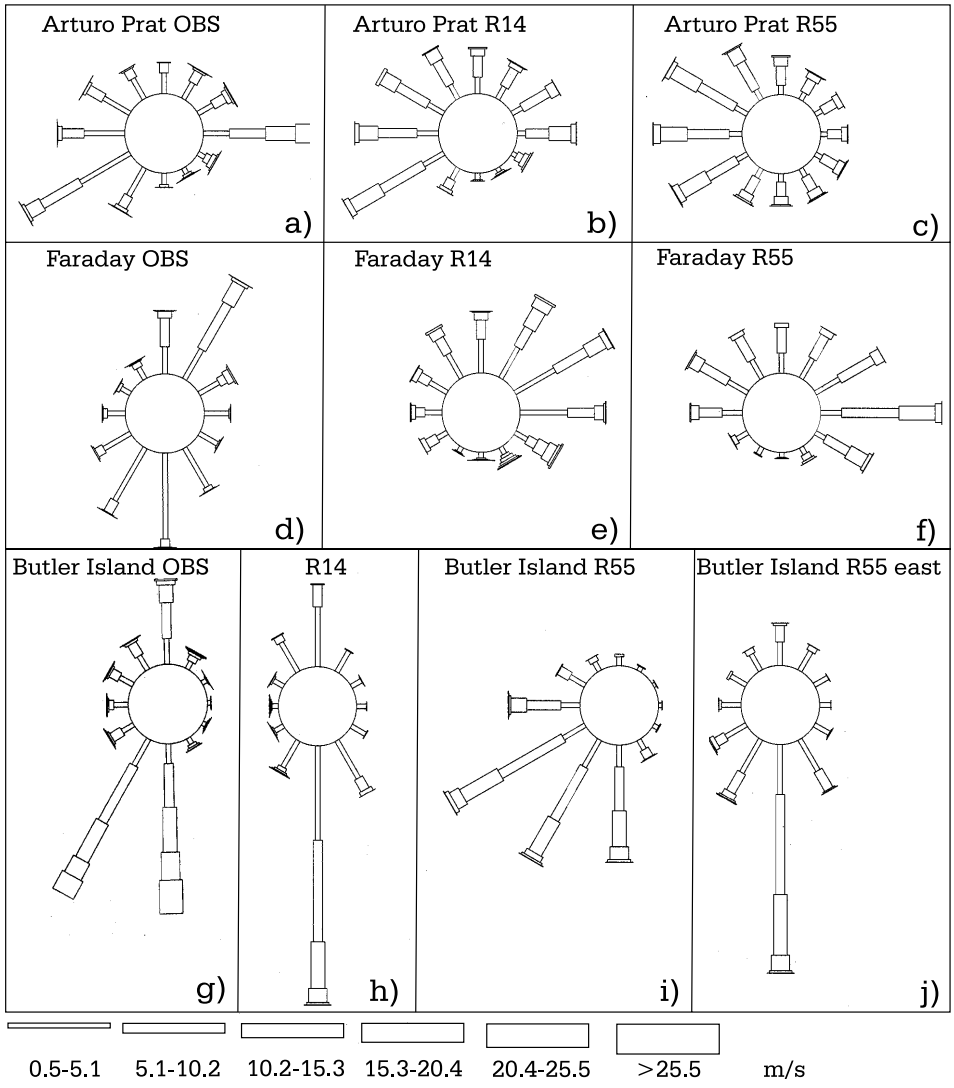


**Figure 9.** Wind roses for (top) Arturo Prat, (middle) Faraday (now Vernadsky), and (bottom) Butler Island, observed at the station and calculated from 6-hour RACMO14 and RACMO55 values for the 7-year period 1987–1993 at the grid boxes corresponding to the measuring site. The wind directions are divided into 30° bins and the wind speeds into 10 knot bins from 1 to 40 knots (1 knot = 0.51 m $s^{-1}$). For Butler Island the wind rose for an additional RACMO55 grid box east of the site is shown.

measurements at the Antarctic station Halley during 67 days of blowing snow conditions between March and November 1991.

$$\begin{aligned} Q &= 0 && \text{for} \quad u_* \le u_{*_t}; \\ Q &= 0.297 \cdot \left(e^{2.805 \cdot (u_* - u_{*t})} - 1\right) && \text{for} \quad u_* > u_{*_t}, \end{aligned} \tag{3}$$

where $Q$ is in kg $m^{-1}$ $s^{-1}$ and $u_*$ in m $s^{-1}$. We use a fixed value for the threshold friction velocity ($u_{*t}$) of 0.3 m $s^{-1}$ as proposed by *Mann et al.* [2000]. Note that we discuss the sensitivity of $Q$ for variations in $u_{*t}$ in Section 4.3. RACMO14 model output, available every 6 hours, is used to calculate $Q$.

[36] Measurements from a snow surface height sensor at the Bryan Coast divide were used to evaluate the model. This site is suitable for studying *SN*, since it is located in a region where the near-surface wind field diverges, and generally, ablation due to snow drift occurs. Ablation events are unambiguously related to *SN*, whereas for accumulation events it is difficult to distinguish $P$ from snow drift accumulation. The height sensor was deployed at an elevation of about 1106 m at 74.4°S, 79.4°W (location shown in Figure 1c) for the period February to December 1999 (Figure 10). The mean measured density at the site in the uppermost two meters of snow (400 kg $m^{-3}$) was used to make the conversion from meters snow to meters water equivalent.

[37] Model output is not available for the year 1999 and therefore we have chosen an arbitrary year (1987) for the evaluation. The annual mean value for $P - E$ is very similar to the total net accumulation measured by the height sensor. However, if *SN* is included in the model, the annual mean net accumulation is underestimated by about 60%.

[38] Periods of constant height can be identified in the measured record; the snow height ($H$) increases because of a

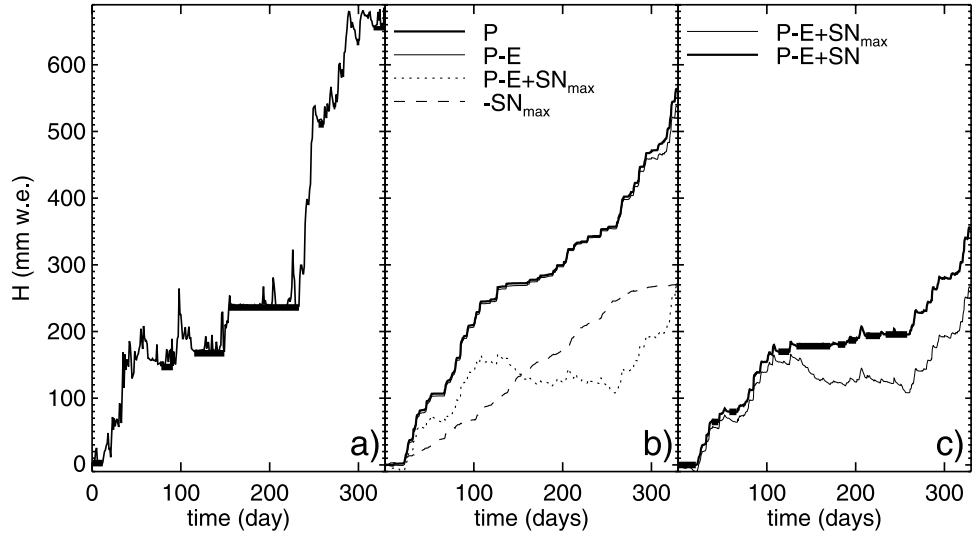


**Figure 10.** (a) Surface mass balance for the year 1999 measured at a site on the divide in the Bryan coast region (location shown in Figure 1c). The thick lines indicate the periods of constant height ($H$) in the record, for example, the period between day 154 and day 233 (see text for further explanation). (b) Precipitation ($P$, thick solid line), precipitation minus sublimation ($P - E$, thin solid line), and precipitation minus sublimation plus snow drift ($P - E + SN_{\max}$, dotted line) and minus snow drift ($-SN_{\max}$, dashed line) for the year 1987 simulated at the RACMO14 grid box closest to the measuring site. (c) Same as Figure 10b but for $P - E + SN_{\max}$ (thin solid line) and $P - E + SN$ (thick solid line), where $SN_{\max}$ is the snow drift calculated directly from *Mann et al.* [2000] using equation (3) and $SN$ is the snow drift calculated from *Mann et al.* [2000] including a period $T_{\max}$ of 7 days maximizing snow removal.

precipitation event but returns to a previously recorded value because of an ablation event related to snow drift and remains at this value until the next accumulation event (e.g., the period between day 154 and day 233). These periods of constant $H$ are absent in the modeled time series: Clearly there is a process, limiting net ablation due to snow drift, that is not taken into account in the parameterization given in equation (3).

[39] To take into account the process limiting $SN$, we allow ablation by snow drift to occur at a rate given by equation (3) until all snow that fell less than $T_{\max}$ days ago has been removed. At this point ablation is set to zero until further snow falls. The reasoning behind this parameterization is that as snow ages it becomes increasingly less erodible as bonds develop between snow crystals. Without the detailed measurements that would be necessary to develop a physically based model of this process, we adopt the simple approach described above.

[40] $T_{\max}$ was chosen in such a way that the number of periods of constant $H$ ($N_H$) in the modeled time series corresponds to $N_H$ derived from the measured time series. All measuring points shown in Figure 10 were binned into 100 $H$ intervals. A period of constant $H$ was identified when $H$ returned to a previously measured value for two or more sequential points. It turned out that $N_H = 8$ for the period February to December 1999. A period ($T_{\max}$) of 7 days gives the best agreement between model and measurements (Figure 10c), which means that snow older than 7 days cannot be removed from the surface by the wind. The $H$ changes in the model are smaller than in the measured record, which might be related to the fact that fresh snow has a lower density than settled snow. Since we use a constant value for the density of 400 kg m$^{-3}$, the converted $H$ changes in the measured record in mm w.e. might be overestimated.

[41] The average accumulation over a period of about 5 years (1995–1999) has been measured along a transect in the Bryan Coast region (Figure 11). Two local maxima in net accumulation are present on the transect, the first one at about 29 km from the coast and the second one at 62 km from the coast. The first maximum is related to a local nunatak which is not represented in the RACMO14 orography (T. A. Lachlan-Cope, British Antarctic Survey, personal communication, 2004) and will therefore be ignored in the model evaluation. Averaged over the transect, RACMO14 $P - E$ corresponds closely to $B_{obs}$. However, the spatial pattern is not correctly represented with the RACMO14 local maximum too close to the coast.

[42] On the transect, ablation due to snow drift occurs. The correspondence between model and measurements, in mean $B$ over the transect, deteriorates by including $SN$. On the other hand, the modeled spatial $P - E + SN$ pattern corresponds more closely to $B_{obs}$ than the modeled spatial $P - E$ pattern. The local $P - E + SN$ maximum is at approximately the same location as the maximum in $B_{obs}$. Interestingly, both $P$ and ablation due to snow drift are largest in the region where the slope is steepest, and therefore the net accumulation in the Bryan Coast region is expected to be smallest at the location where $P$ is largest.

### 3.4. Precipitation, Sublimation, and Snow Drift

[43] Since $SN$ is largely controlled by the near-surface wind field, we present this variable in Figure 12a. The

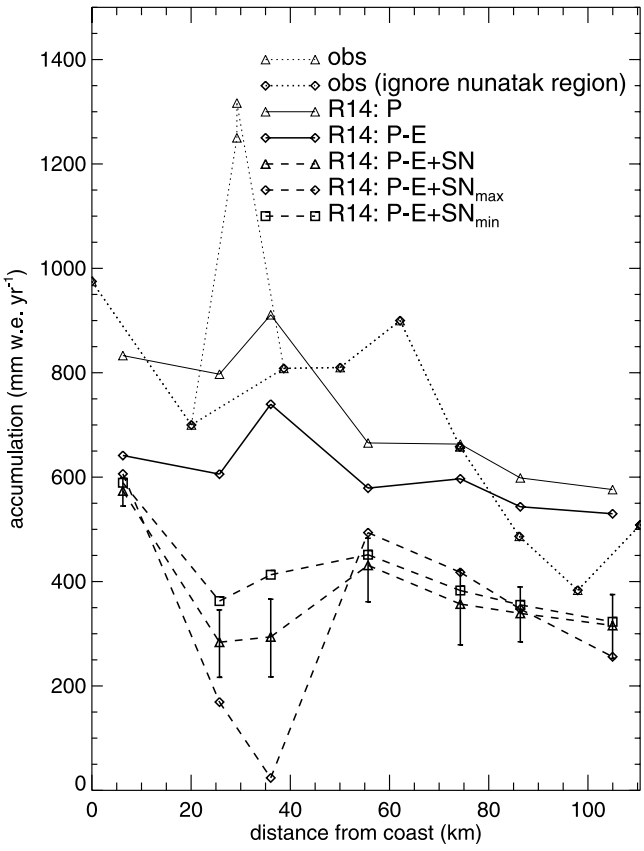


**Figure 11.** Observed (1995–1999) and modeled (1987–1993) average surface mass balance on the transect going from the height sensor (location shown in Figure 1c) toward the coast. The lines indicate the observations (thin dotted line), observations ignoring a nunatak region where local effects might play a role (thick dotted line), modeled precipitation ($P$, thin solid line), modeled precipitation minus sublimation ($P - E$, thick solid line), modeled precipitation minus sublimation plus snow drift ($P - E + SN$, dashed line with triangles), modeled precipitation minus sublimation plus snow drift calculated directly using equation (3) ignoring time limit for removal of snow ($P - E + SN_{\max}$, dashed line with diamonds), modeled precipitation minus sublimation plus snow drift maximizing the wind speed on 20 m s$^{-1}$ ($P - E + SN_{\min}$, dashed line with squares). The error bars show the sensitivity of the modeled surface mass balance for variations in the threshold friction velocity of 0.1 m s$^{-1}$ around the central value of 0.3 m s$^{-1}$.

7-year mean near-surface wind field is strongly controlled by the orography. Near the coast, the barrier effect can be identified with northerlies prevailing on the western side and southerlies on the eastern side of the AP. Note that a 180° rotation of the wind occurs frequently near the coast, establishing the bimodal wind distribution as can be seen in Figure 9. Katabatic winds strongly control the near-surface wind field over the land ice. The winds are stronger on the eastern side of the AP than on the western side because of downward transport of momentum in lee waves.

[44] Local divergence of the wind field on the spine implies the removal of snow from the spine region (Figure 12b). This is in correspondence with *Turner et al.* [2002], who identified the spine as a region where $SN$ is possibly large. Most of the snow, transported away from the spine, is deposited on the eastern side thereby reducing the east-west gradient of $B_{mod}$. Removal of snow by the wind also occurs on top of the northern mountains of Alexander Island. Also on Berkner Island (not shown), snow appears to be removed from the top of the domes, with snow deposition mainly occurring on the western side of the island.

[45] The modeled surface mass balance, defined as $P - E + SN$, is shown in Figure 12c. The distribution of $P - E + SN$ is similar to $P - E$ presented in Figure 3b: The largest values are found over the western steep slopes of the AP. The net accumulation on the northern spine is smaller and net accumulation on the eastern side of the AP is larger when $SN$ is included in the calculations. The spatial variability on a transect over the spine of the AP is much larger for $P - E + SN$ than for $P - E$, showing that it is difficult to interpolate sparse measurements in this region, where $SN$ apparently plays a large role. Note that the spatial variability of $P - E + SN$ is probably even larger on a scale smaller than the 14-km scale that we have used in our integrations.

[46] The inclusion of $SN$ in $B_{mod}$ deteriorates the correspondence between model and in situ observations presented in Figure 4. When $P - E$ is compared with the in situ measurements, $\langle|\Delta B|\rangle$ is 220 mm w.e. yr$^{-1}$. When $SN$ is included, $\langle|\Delta B|\rangle$ is 245 mm w.e. yr$^{-1}$.

[47] The average calculated precipitation over the region of the AP, as defined in Section 3.1, is 1.20 m w.e. yr$^{-1}$. We estimated that about 0.11 m w.e. yr$^{-1}$ (9% of $P$) is removed from the AP because of surface sublimation and 0.06 m w.e. yr$^{-1}$ (5%) is removed because of wind transport of snow over the grounding line toward the sea.

## 4. Discussion

### 4.1. Precipitation Over Land

[48] It is generally known that there is a strong effect of the orography on the long-term mean distribution of $P$. When air is lifted over a barrier, it cools as it rises, causing condensation and precipitation. These processes are represented by the model, resulting in high values for $P$ on the northwestern slopes of the AP.

[49] Microphysical processes, like the seeder-feeder mechanism where an upper level cloud feeds an orographically induced lower-level cloud with ice crystals [*Smith*, 1979], are relevant for the spatial distribution of $P$ in mountainous regions. In addition, the time delay between condensation and precipitation reaching the surface is of importance for the spatial distribution of $P$ [*Colle*, 2004]. Three timescales are relevant namely the advection timescale ($\tau_a$), the fallout timescale ($\tau_f$) and the snow generation timescale ($\tau_{cs}$) [*Jiang and Smith*, 2003]. The timescales $\tau_a$ and $\tau_{cs}$ are taken into account: The model allows for advection of the condensation before $P$ is formed. The third timescale $\tau_f$ is not taken into account; precipitation is a diagnostic model variable and advection of precipitation is not included in the model. This might result in a westward displacement of $P$ in the model.

[50] We estimated the order of magnitude of the westward displacement by using an estimate for $\tau_f$ of 1000s [*Jiang*

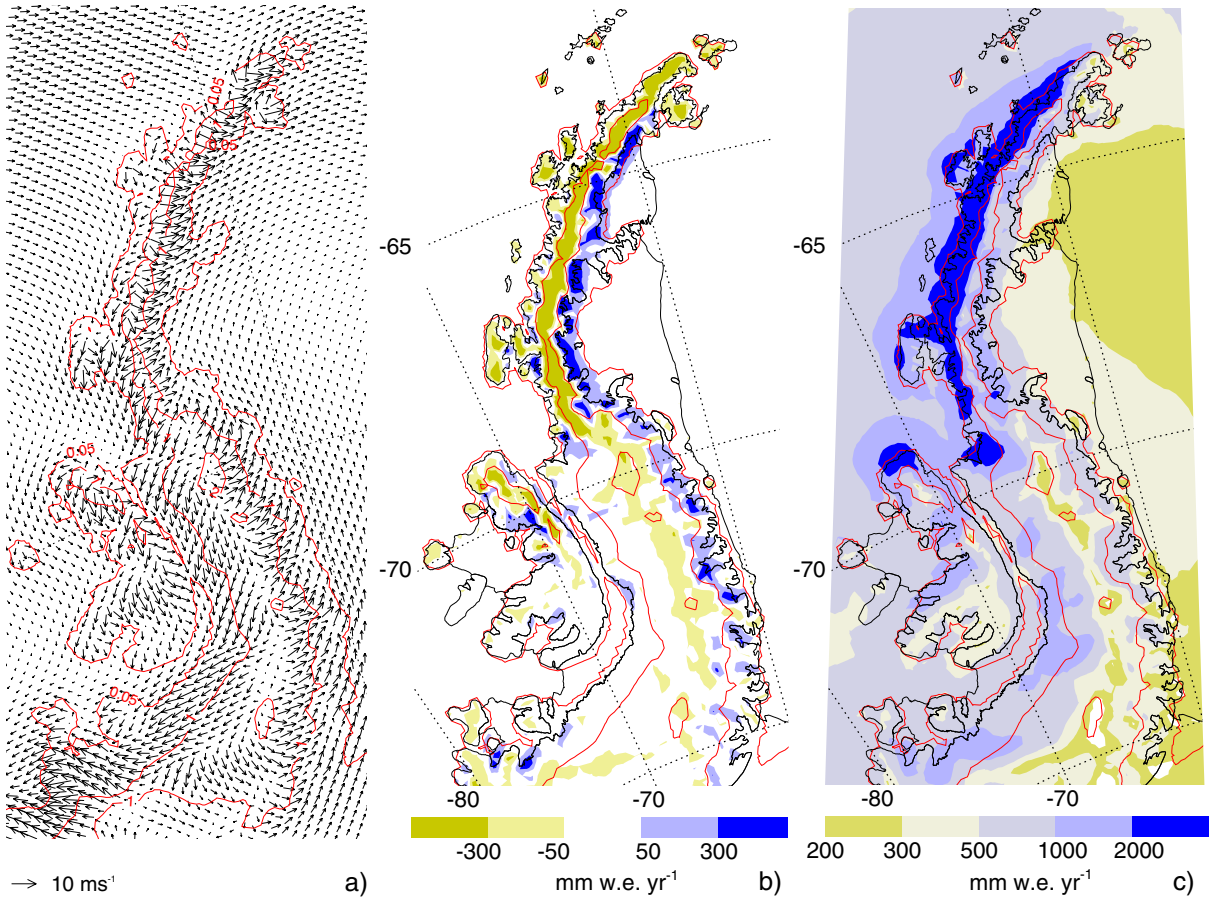


**Figure 12.** Modeled 7-year mean (a) near-surface wind field at the lowest model level (about 7 m height above the surface), (b) accumulation (blue) or ablation (yellow) due to transport of snow by the wind, and (c) precipitation minus sublimation plus snow drift. Black contour lines indicate the edge of the ice shelf and the grounding line. Red contour lines are plotted at model surface elevations of 50 m, 1 km, and 2 km.

*and Smith*, 2003] and an estimate of the wind speed during precipitation events;

$$|\vec{u}|_{\text{precip}} = \frac{\sum_{i=1,n} |\vec{u}_i| P_i}{\sum_{i=1,n} P_i}, \tag{4}$$

where $|\vec{u}_i|$ is the wind speed at time $i$, $P_i$ is the precipitation over 6 hours at time $i$, and $n$ is the number of 6-hour time intervals during the 7-year time period (model output is available every 6 hours). At Faraday, $|\vec{u}|_{\text{precip}}$ at 1 km height is 15 m s$^{-1}$. The length of the modeled 7-year mean wind vector weighted with the precipitation is 12 m s$^{-1}$. It is therefore plausible that $P$ is, on average, advected over a distance of about the size of a grid box (14 km). Therefore the westward displacement of the maximum in $P$ is of the order of the size of a grid box.

[51] There are no measurements from the western slopes of the AP to check whether or not a westward displacement is simulated. Comprehensive data sets of $P$ are available for orographic barriers in other regions of the world. Precipitation is found to be heaviest on the lower windward slopes and decreases toward higher terrain in the European Alps [*Houze et al.*, 2001; *Frei and Schär*, 1998] and in the Olympic mountains in Washington [*Mass and Ferber*, 1990]. On the other hand, precipitation is heaviest over the crest in the Coast Range and Cascade Range in Oregon [*Daly et al.*, 1994]. It is therefore not clear where exactly the maximum in $P$ on the barrier of the AP can be expected.

[52] We recommend that additional measurements of $B$ are performed on the western slopes and the spine of the AP to investigate the location of the maximum in $P$ in more detail. In addition, future modeling of $P$ over the AP should include a more detailed parameterization of $P$, including cloud microphysical processes and downstream advection of precipitation.

### 4.2. Precipitation Over Sea

[53] The uplift of air over the Bellingshausen Sea, west of the AP, affects the distribution of $P$ over this region. The input of fresh water into the ocean is found to be about 1.5 m w.e. yr$^{-1}$, a value comparable to the basal melt

of George VI Ice Shelf [*Potter and Paren*, 1985]. They estimated the basal melt of George VI Ice Shelf to be in between 1.1 and 3.6 m w.e. $yr^{-1}$, which is about one sixth of the total basal melt in Antarctica. Model results indicate that the precipitation input north west of the AP is an important contribution to the total freshwater input in this region.

[54] A strong gradient in $P$ exists over the ocean north west of the AP. The modeled $P$ decreases from 1.5 m w.e. $yr^{-1}$ near the coast to 1 m w.e. $yr^{-1}$ at a distance of 80 km from the coast. This gradient in $P$ induces a density gradient in the ocean, which might have an effect on the ocean circulation in this region. The geostrophic flow associated with the density gradient, calculated assuming the freshwater is evenly mixed over the upper 50 m of the water column, is of the order of magnitude of 1 cm $s^{-1}$.

### 4.3. Snow Drift

[55] We allow ablation by snow drift to occur at a rate given by equation (3) until all snow that fell less than 7 days ago has been removed. This empirical relation (equation (3)) was derived using measurements from the coastal station Halley (75.6°S, 26.7°W). In this equation, the friction velocity needs to be larger than a certain threshold value ($u_{*t}$ = 0.3 m $s^{-1}$), before transport takes places. *Gallée et al.* [2001] showed that $u_{*t}$ is dependent on the snow type and temperature. In large parts of the AP, the annual mean near-surface temperature is within 5°C of the annual mean near-surface temperature at Halley (−19°C), except near the coast in the northern part of the AP, where temperatures are higher than the temperatures at Halley.

[56] The sensitivity for variations in $u_{*t}$ has been tested and the result is shown in Figure 11. The error bars in this plot indicate the sensitivity of $B_{mod}$ for variations in $u_{*t}$ of 0.1 m $s^{-1}$ around the central value of 0.3 m $s^{-1}$. By decreasing (increasing) $u_{*t}$ in equation (3) to 0.2 m $s^{-1}$ (0.4 m $s^{-1}$) the ablation due to snow drift increases (decreases). Therefore the average $P - E + SN$ on the transect decreases (increases) by 17% (15%). The shape of the curve in Figure 11 and the spatial pattern of $SN$ over the AP are not affected by changing $u_{*t}$. The wind driven transport of snow over the grounding line toward the sea is 6 ± 1% of $P$, for $u_{*t}$ = 0.3 ± 0.1 m $s^{-1}$.

[57] Two other uncertainties in the calculation of $SN$ are i) the time period maximizing snow removal ($T_{\max}$), and ii) $SN$ at wind speeds larger than 20 m $s^{-1}$. Halley is a site with moderate wind speeds, so the empirical relation that was used to calculate $SN$ (equation (3)) is derived from measurements up to a wind speed of 20 m $s^{-1}$. For this reason, we have performed two sensitivity calculations; i) $T_{\max} = \infty$, and ii) the wind speed in the calculation of $SN$ is limited to 20 m $s^{-1}$.

[58] The sensitivity for $T_{\max}$ is large (Figure 11). When $T_{\max} = \infty$, more snow is removed especially in the region from 25 km to 45 km from the coast. At 36 km from the coast $B_{mod}$ is zero which is unrealistic, since no blue ice areas (where $B$ is negative) are observed in this region.

[59] The sensitivity of $SN$ to the uncertainty of equation (3) at wind speeds above 20 m $s^{-1}$ is small (Figure 11). This implies that in the Bryan Coast, $SN$ is not very sensitive for the transport at wind speeds larger than 20 m $s^{-1}$. Uncertainties in the high wind speed limit of the empirical relation do not affect the uncertainties in the calculated value for $SN$ in this region.

[60] Snow drift affects the spatial distribution of $B$. On the spine of the AP, on local domes (e.g., Berkner Island), on divides and on peaks (e.g., mountain tops on Alexander Island), ablation due to snow drift occurs and $B$ is smaller than $P - E$. The blowing snow deposits at lower elevations. Generally, wind transports snow away from local mountain tops, spines and domes. Since ice cores are often collected on divides or local domes, accumulation derived from these cores might not be representative for the average accumulation over a larger domain, and therefore area-averaged estimates of $B$, based on these measurements, might be underestimated.

## 5. Conclusions

[61] A regional atmospheric model (grid spacing $\Delta x$ = 14 km), nested in a coarser resolution integration ($\Delta x$ = 55 km), is used to study the surface mass balance in the Antarctic Peninsula region. In contrast to *Turner et al.* [2002], who identify the northern spine as the region with the highest value for $B$, we find the highest values on the northwestern slopes of the AP. Although measurements are too sparse to verify the spatial distribution of $B_{mod}$, the physical mechanism responsible for the spatial distribution of $B_{mod}$ is represented in the model: Upward motion of air is found on the western side of the barrier, resulting in high precipitation. Note that these heavy precipitation events occur mainly during unblocked flow conditions when the Froude number is larger than unity. During blocked conditions, the flow is deviated around the northern tip of the AP, resulting in dry conditions on the AP.

[62] We found an improvement of the simulated wind field by decreasing $\Delta x$ from 55 km to 14 km, which is relevant for the parameterization of $SN$. A resolution of 14 km is fine enough to capture barrier wind effects at coastal stations (e.g., Butler Island).

[63] From height sensor measurements in the Bryan Coast region it appears that parameterizations of $SN$ from literature [e.g., *Mann et al.*, 2000], which calculate the transport as a function of near-surface wind speed or friction velocity, lack a process limiting $SN$. Without the detailed measurements that would be necessary to develop a physically based model of this process, we adopt a simple approach to include the effects of the process limiting ablation of older snow by the wind. Implementation of this parameterization improves the correspondence between height sensor measurements and modeled time series.

[64] The sum of $P$, $E$ and $SN$, averaged over the 200 measuring sites, is about 10% lower than $B_{obs}$ at the sites. Taking into account melt and sublimation of blowing snow, would further reduce the net accumulation in the model, making the discrepancy between model and measurements larger than 10%. The model bias is largely caused by the overestimation of the precipitation shadow of Alexander Island, where in situ measurements are dense.

[65] The AP is defined as the region north of a line joining Cape Adams and a point (73°24′S, 72°00′W) on the English coast [*Aagaard*, 1930] (see Figure 1b). Our estimate for the mean surface mass balance is 1.04 m w.e. $yr^{-1}$, which corresponds to a net mass input on the AP of

280 Gt $yr^{-1}$, a value 12% larger than we found previously in the RACMO55 integrations. Precipitation is the largest surface mass balance component, whereas the mean value for *E* and *SN* over the AP are estimated to be 0.1 m w.e. $yr^{-1}$ and −0.06 to −0.08 m w.e. $yr^{-1}$, respectively, which is 1 order of magnitude smaller than *P*.

[66] **Acknowledgments.** We would like to thank scientists from British Antarctic Survey (BAS) for their valuable comments on this topic. In especially Adrian Jenkins and Keith Nicholls are thanked for discussions on the ocean circulation. We would like to thank scientists from the Royal Netherlands Meteorological Institute (KNMI) in especially Geert Lenderink and Sander Tijm for their help on interpretation of the output from the high-resolution integration. We are grateful to three anonymous reviewers, whose detailed comments greatly improved the paper. This work was supported by the European Commission under a Marie Curie Fellowship and by the Computer Services for Academic Research (CSAR) for the use of High-Performance Computing facilities.

## References

Aagaard, B. (1930), Fangst og forskning i Sydishavet, Oslo, *Gyldendal Norsk Forland*, vol. 1, 162 pp., Gyldendal Norsk Forlag, Oslo.

Bintanja, R., and C. H. Reijmer (2001), A simple parameterization for snowdrift sublimation over Antarctic snow surfaces, *J. Geophys. Res.*, *106*(D23), 31,739–31,748.

Box, J. E., and A. Rinke (2003), Evaluation of Greenland ice sheet surface climate in the HIRHAM regional climate model, *J. Clim.*, *16*, 1302–1319.

Christensen, J. H., and E. Van Meijgaard (1992), On the construction of a regional atmospheric climate model, *Tech. Rep. 147*, 22 pp., R. Neth. Meteorol. Inst., de Bilt, Netherlands.

Christensen, J. H., O. B. Christensen, P. Lopez, E. Van Meijgaard, and M. Botzet (1996), The HIRHAM4 regional atmospheric climate model, *DMI Sci. Rep. 96-4*, 51 pp., Dan. Meteorol. Inst., Copenhagen, Denmark.

Colle, B. A. (2004), Sensitivity of orographic precipitation to changing ambient conditions and terrain geometries: An idealized modeling perspective, *J. Atmos. Sci.*, *61*, 588–606.

Colle, B. A., and C. F. Mass (1996), An observational and modeling study of the interaction of low-level southwesterly flow with the Olympic Mountains during COAST IOP 4, *Mon. Weather Rev.*, *124*, 2152–2175.

Daly, C., R. P. Neilson, and D. L. Phillips (1994), A statistical topographic model for mapping climatological precipitation over mountainous terrain, *J. Appl. Meteorol.*, *33*(2), 140–158.

Davies, H. C. (1976), A lateral boundary formulation for multi-level prediction models, *Q. J. R. Meteorol. Soc.*, *102*, 405–418.

Déry, S. J., and M. K. Yau (2002), Large-scale mass balance effects of blowing snow and surface sublimation, *J. Geophys. Res.*, *107*(D23), 4679, doi:10.1029/2001JD001251.

Durran, D. R., and J. B. Klemp (1982), On the effects of moisture on the Brunt-Väisälä frequency, *J. Atmos. Sci.*, *39*, 2152–2158.

Frei, C., and C. Schär (1998), A precipitation climatology of the Alps from high-resolution rain-gauge observations, *Int. J. Climatol.*, *18*(8), 873–900.

Frei, C., J. H. Christensen, M. Deque, D. Jacob, R. G. Jones, and P. L. Vidale (2003), Daily precipitation statistics in regional climate models: Evaluation and intercomparison for the European Alps, *J. Geophys. Res.*, *108*(D3), 4124, doi:10.1029/2002JD002287.

Gallée, H., G. Guyomarc'h, and E. Brun (2001), Impact of snow drift on the Antarctic ice sheet surface mass balance: Possible sensitivity to snow-surface properties, *Boundary Layer Meteorol.*, *99*, 1–19.

Houze, R. A., C. N. James, and S. Medina (2001), Radar observations of precipitation and airflow on the Mediterranean side of the Alps: Autumn 1998 and 1999, *Q. J. R. Meteorol. Soc.*, *127*, 2537–2558.

Jiang, Q. F., and R. B. Smith (2003), Cloud timescales and orographic precipitation, *J. Atmos. Sci.*, *60*, 1543–1559.

Katzfey, J. J. (1995), Simulation of extreme New Zealand precipitation events: 1. Sensitivity to orography and resolution, *Mon. Weather Rev.*, *123*, 737–754.

Kiilsholm, S., J. H. Christensen, K. Dethloff, and A. Rinke (2003), Net accumulation of the Greenland ice sheet: High resolution modeling of climate changes, *Geophys. Res. Lett.*, *30*(9), 1485, doi:10.1029/2002GL015742.

King, J. C. (1994), Recent climate variability in the vicinity of the Antarctic Peninsula, *Int. J. Climatol.*, *14*(4), 357–369.

King, J. C., and J. C. Comiso (2003), The spatial coherence of interannual temperature variations in the Antarctic Peninsula, *Geophys. Res. Lett.*, *30*(2), 1040, doi:10.1029/2002GL015580.

King, J. C., P. S. Anderson, M. C. Smith, and S. D. Mobbs (1996), The surface energy and mass balance at Halley, Antarctica during winter, *J. Geophys. Res.*, *101*(D14), 19,119–19,128.

Lenderink, G., and E. Van Meijgaard (2001), Impacts of cloud and turbulence schemes on integrated water vapor: Comparison between model predictions and GPS measurements, *Meteorol. Atmos. Phys.*, *77*, 131–144.

Lenderink, G., et al. (2004), The diurnal cycle of shallow cumulus clouds over land: A single column model intercomparison study, *Q. J. R. Meteorol. Soc.*, in press.

Mann, G. W., P. S. Anderson, and S. D. Mobbs (2000), Profile measurements of blowing snow at Halley, Antarctica, *J. Geophys. Res.*, *105*(D19), 24,491–24,508.

Marshall, G. J. (2000), An examination of the precipitation regime at Thurston Island, Antarctica, from ECMWF re-analysis data, *Int. J. Climatol.*, *20*(3), 255–277.

Marshall, G. J. (2002), Analysis of recent circulation and thermal advection change in the northern Antarctic Peninsula, *Int. J. Climatol.*, *22*(12), 1557–1567.

Marshall, G. J., V. Lagun, and T. A. Lachlan-Cope (2002), Changes in Antarctic Peninsula tropospheric temperatures from 1956 to 1999: A synthesis of observations and reanalysis data, *Int. J. Climatol.*, *22*(3), 291–310.

Mass, C. F., and G. K. Ferber (1990), Surface pressure perturbations produced by an isolated mesoscale topographic barrier: 1. General-characteristics and dynamics., *Mon. Weather Rev.*, *118*, 2579–2596.

Mass, C. F., D. Ovens, K. Westrick, and B. A. Colle (2002), Does increasing horizontal resolution produce more skillful forecasts? The results of two years of real-time numerical weather prediction over the Pacific northwest, *Bull. Am. Meteorol. Soc.*, *83*(3), 407–430.

Orr, A., D. Cresswell, G. J. Marshall, J. C. R. Hunt, J. Sommeria, C. G. Wang, and M. Light (2004), A "low-level" explanation for the recent large warming trend over the western Antarctic Peninsula involving blocked winds and changes in zonal circulation, *Geophys. Res. Lett.*, *31*, L06204, doi:10.1029/2003GL019160.

Parish, T. R. (1982), Barrier winds along the Sierra-Nevada mountains, *J. Appl. Meteorol.*, *21*(7), 925–930.

Pascoe, C. L. (2002), Cyclolysis and cyclogenesis at the Antarctic Peninsula, Ph.D. thesis, 186 pp., Univ. of Leeds, Leeds, U. K.

Peel, D. A. (1992), Ice core evidence from the Antarctic Peninsula region, in *Climate Since A.D. 1500*, edited by R. S. Bradley and P. D. Jones, pp. 549–571, Routledge, New York.

Potter, J. R., and J. G. Paren (1985), Interaction between ice shelf and ocean in George VI sound, Antarctica, in *Oceanology of the Antarctic Continental Shelf*, *Antarct. Res. Ser.*, vol. 43, edited by S. S. Jacobs, pp. 35–58, AGU, Washington D. C.

Reijmer, C. H., E. van Meijgaard, and M. R. van den Broeke (2004), Numerical studies with a regional atmospheric climate model based on changes in the roughness length for momentum and heat over Antarctica, *Boundary Layer Meteorol.*, *111*, 313–337.

Roeckner, E., K. Arpe, L. Bengtsson, M. Christoph, M. Claussen, L. Dümenil, M. Esch, M. Giorgetta, U. Schlese, and U. Schulzweida (1996), The atmospheric general circulation model ECHAM-4: Model description and simulation of present-day climate, *Rep. 218*, Max-Planck Inst. für Meteorol., Hamburg, Germany.

Skvarca, P., W. Rack, H. Rott, and T. I. Y. Donangelo (1999), Climatic trend and the retreat and disintegration of ice shelves on the Antarctic Peninsula: An overview, *Polar Res.*, *18*(2), 151–157.

Smith, R. B. (1979), The influence of mountains on the atmosphere, *Adv. Geophys.*, *21*, 87–230.

Sundqvist, H. (1978), A parameterization scheme for non-convective condensation including prediction of cloud water content., *Q. J. R. Meteorol. Soc.*, *104*, 677–690.

Turner, J., S. R. Colwell, and S. Harangozo (1997), Variability of precipitation over the coastal western Antarctic Peninsula from synoptic observations, *J. Geophys. Res.*, *102*(D12), 13,999–14,007.

Turner, J., W. M. Connolley, S. Leonard, G. J. Marshall, and D. G. Vaughan (1999), Spatial and temporal variability of net snow accumulation over the Antarctic from ECMWF re-analysis project data, *Int. J. Climatol.*, *19*(7), 697–724.

Turner, J., T. A. Lachlan-Cope, G. J. Marshall, E. M. Morris, R. Mulvaney, and W. Winter (2002), Spatial variability of Antarctic Peninsula net surface mass balance, *J. Geophys. Res.*, *107*(D13), 4173, doi:10.1029/2001JD000755.

Turner, J., S. R. Colwell, G. J. Marshall, T. A. Lachlan-Cope, A. M. Carleton, P. D. Jones, V. Lagun, P. A. Reid, and S. Iagovkina (2004), The SCAR READER project: Towards a high-quality database of mean Antarctic meteorological observations, *J. Clim.*, *17*, 2890–2898.

van den Broeke, M. R., and R. Bintanja (1995), The interaction of katabatic wind and the formation of blue ice areas in East Antarctica, *J. Glaciol.*, *41*, 395–407.

van den Broeke, M. R., and N. P. M. van Lipzig (2003), Response of wintertime Antarctic temperatures to the Antarctic Oscillation: Results of a regional climate model, in *Antarctic Peninsula Climate Variability: A Historical and Paleoenvironmental Perspective*, *Antarct. Res. Ser.*, vol. 79, edited by E. Domack et al., pp. 43–58, AGU, Washington, D. C.

van Lipzig, N. P. M., E. van Meijgaard, and J. Oerlemans (1999), Evaluation of a regional atmospheric climate model using measurements of surface heat exchange processes from a site in Antarctica, *Mon. Weather Rev.*, *127*, 1994–2001.

van Lipzig, N. P. M., E. van Meijgaard, and J. Oerlemans (2002a), The effect of temporal variations in the surface mass balance and temperature-inversion strength on the interpretation of ice-core signals, *J. Glaciol.*, *48*, 611–621.

van Lipzig, N. P. M., E. van Meijgaard, and J. Oerlemans (2002b), The spatial and temporal variability of the surface mass balance in Antarctica: Results from a regional atmospheric climate model, *Int. J. Climatol.*, *22*(10), 1197–1217.

Vaughan, D. G., and C. S. M. Doake (1996), Recent atmospheric warming and retreat of ice shelves on the Antarctic Peninsula, *Nature*, *379*(6563), 328–331.

Werner, M., U. Mikolajewicz, M. Heimann, and G. Hoffmann (2000), Borehole versus isotope temperatures on Greenland: Seasonality does matter, *Geophys. Res. Lett.*, *27*(5), 723–726.

Wu, Y. H., S. Raman, U. C. Mohanty, and R. V. Madala (2002), Sensitivity of monsoon circulation and precipitation over India to model horizontal resolution and orographic effects, *Meteorol. Appl.*, *9*(3), 345–356.

J. C. King and T. A. Lachlan-Cope, British Antarctic Survey, High Cross, Madingley Road, Cambridge CB3 0ET, UK.

M. R. van den Broeke, Institute for Marine and Atmospheric Research, Utrecht University, PO Box 80 005, NL-3508 TA Utrecht, Netherlands.

N. P. M. van Lipzig, Meteorological Institute, University of Munich, Theresienstr. 37, D-80333 Munich, Germany. (nicole@meteo.physik.uni-muenchen.de)